

# The Blue Straggler Population of the Globular Cluster M5 <sup>1</sup>

B. Lanzoni<sup>1,2</sup>, E. Dalessandro<sup>1,2</sup>, F.R. Ferraro<sup>1</sup>, C. Mancini<sup>3</sup>, G. Beccari<sup>2,4,5</sup>, R.T. Rood<sup>6</sup>,  
M. Mapelli<sup>7</sup>, S. Sigurdsson<sup>8</sup>

<sup>1</sup> *Dipartimento di Astronomia, Università degli Studi di Bologna, via Ranzani 1, I-40127 Bologna, Italy*

<sup>2</sup> *INAF-Osservatorio Astronomico di Bologna, via Ranzani 1, I-40127 Bologna, Italy*

<sup>3</sup> *Dipartimento di Astronomia e Scienza dello Spazio, Università degli Studi di Firenze, Largo Enrico Fermi 2, I- 50125 Firenze, Italy*

<sup>4</sup> *Dipartimento di Scienze della Comunicazione, Università degli Studi di Teramo, Italy*

<sup>5</sup> *INAF-Osservatorio Astronomico di Collurania, Via Mentore Maggini, I-64100 Teramo, Italy*

<sup>6</sup> *Department of Astronomy and Astrophysics, The Pennsylvania State University, 525 Davey Lab, University Park, PA 16802*

<sup>7</sup> *S.I.S.S.A., Via Beirut 2 - 4, I-34014 Trieste, Italy*

<sup>8</sup> *Astronomy Department, University of Virginia, P.O. Box 400325, Charlottesville, VA, 22904*

20 March, 07

## ABSTRACT

By combining high-resolution HST and wide-field ground based observations, in ultraviolet and optical bands, we study the Blue Stragglers Star (BSS) population of the galactic globular cluster M5 (NGC 5904) from its very central regions up to its periphery. The BSS distribution is highly peaked in the cluster center, decreases at intermediate radii and rises again outward. Such a bimodal distribution is similar to those previously observed in other globular clusters (M3, 47 Tucanae, NGC 6752). As for these clusters, dynamical simulations suggest that, while the majority of BSS in M5 could be originated by stellar collisions, a significant fraction (20-40%) of BSS generated by mass transfer processes in primordial binaries is required to reproduce the observed radial distribution. A candidate BSS has been detected beyond the cluster tidal radius. If confirmed, this could represent an interesting case of an "evaporating" BSS.

*Subject headings:* Globular clusters: individual (M5); stars: evolution – binaries:  
general - blue stragglers

## 1. INTRODUCTION

In globular cluster (GC) color-magnitude diagrams (CMD) blue straggler stars (BSS) appear to be brighter and bluer than the Turn-Off (TO) stars and lie along an extension of the Main Sequence. Since BSS mimic a rejuvenated stellar population with masses larger than the normal cluster stars (this is also confirmed by direct mass measurements; e.g. Shara et al. 1997), they are thought to be objects that have increased their initial mass during their evolution by means of some process. Two main scenarios have been proposed for their formation: the *collisional scenario* suggests that BSS are the end-products of stellar mergers induced by collisions (COL-BSS), while in the *mass-transfer* scenario BSS form by the mass-transfer activity between two companions in a binary system (MT-BSS), possibly up to the complete coalescence of the two stars. Hence, understanding the origin of BSS in stellar clusters provides valuable insight both on the binary evolution processes and on the effects of dynamical interactions on the (otherwise normal) stellar evolution.

The relative efficiency of the two formation mechanisms is thought to depend on the environment (Fusi Pecci et al. 1992; Ferraro et al. 1999a; Bellazzini et al. 2002; Ferraro et al. 2003). COL-BSS are expected to be formed preferentially in high-density environments (i.e., the GC central regions), where stellar collisions are most probable, and MT-BSS should mainly populate lower density environments (the cluster peripheries), where binary systems can more easily evolve in isolation without suffering exchanges or ionization due to gravitational encounters. The overall scenario is complicated by the fact that primordial binaries can also sink to the core due to mass segregation processes, and “new” binaries can be formed in the cluster centers by gravitational encounters. The two formation mechanisms are likely to be at work simultaneously in every GC (see the case of M3 as an example; Ferraro et al. 1993, 1997), but the identification of the cluster properties that mainly affect their relative efficiency is still an open issue.

One possibility for distinguishing between the two types of BSS is offered by high-resolution spectroscopic studies. Anomalous chemical abundances are expected at the surface

---

<sup>1</sup>Based on observations with the NASA/ESA HST, obtained at the Space Telescope Science Institute, which is operated by AURA, Inc., under NASA contract NAS5-26555. Also based on WFI observations collected at the European Southern Observatory, La Silla, Chile, within the observing programs 62.L-0354 and 64.L-0439.

of BSS resulting from MT activity (Sarna & de Greve 1996), while they are not predicted in case of a collisional formation (Lombardi, Rasio & Shapiro 1995). Such studies have just become feasible, and the results found in the case of 47 Tucanae (47 Tuc; Ferraro et al. 2006a) are encouraging. The detection of unexpected properties of stars along standard evolutionary sequences (e.g., variability, anomalous population fractions, or peculiar radial distributions) can help estimating the fraction of binaries within a cluster (see, e.g., Bailyn 1994; Albrow et al. 2001; Bellazzini et al. 2002; Beccari et al. 2006), but such evidence does not directly allow the determination of the relative efficiency of the two BSS formation processes.

The most widely applicable tool to probe the origin of BSS is their radial distribution within the clusters (see Ferraro 2006, for a review). This has been observed to be *bimodal* (i.e., highly peaked in the cluster centers and peripheries, and significantly lower at intermediate radii) in at least 4 GCs: M3 (Ferraro et al. 1997), 47 Tuc (Ferraro et al. 2004), NGC 6752 (Sabbi et al. 2004), and M5 (Warren, Sandquist & Bolte 2006, hereafter W06). Preliminary evidence of bimodality has also been found in M55 (Zaggia, Piotto & Capaccioli 1997). Dynamical simulations suggest that the bimodal radial distributions observed in M3, 47 Tuc and NGC 6752 (Mapelli et al. 2004, 2006) result from  $\sim 40 - 50\%$  of MT-BSS with the balance being COL-BSS. In this context, the case of  $\omega$  Cen is atypical: the BSS radial distribution in this cluster is flat (Ferraro et al. 2006b), and mass segregation processes have not yet played a major role, thus implying that this system is populated by a vast majority of MT-BSS (Mapelli et al. 2006). These results demonstrate that detailed studies of the BSS radial distribution within GCs are very powerful tools for better understanding the complex interplay between dynamics and stellar evolution in dense stellar systems.

In the present paper we extend this kind of investigation to M5 (NGC 5904). With HST-WFPC2 and -ACS ultraviolet and optical high-resolution images of the core we have been able to efficiently detect the BSS population even in the severely crowded central regions. Moreover, with wide-field optical observations performed with ESO-WFI we sampled the entire cluster extension. The combination of these two data sets allowed us to study the dynamical properties of M5, accurately redetermining its center of gravity, its surface density profile, and the BSS radial distribution over the entire cluster. The BSS population of M5 has been recently studied by W06, but we have extended the analysis to larger distances from the cluster center, and we have used Monte-Carlo dynamical simulations to interpret the observational results.

## 2. OBSERVATIONS AND DATA ANALYSIS

### 2.1. The data sets

The present study is based on a combination of two different photometric data sets:

1. *The high-resolution set* – It consists of a series of ultraviolet (UV) and optical images of the cluster center obtained with HST-WFPC2 (Prop. 6607, P.I. Ferraro). To efficiently resolve the stars in the highly crowded central regions, the Planetary Camera (PC, being the highest resolution instrument:  $0''.046/\text{pixel}$ ) has been pointed approximately on the cluster center, while the three Wide Field Cameras (WF, having a lower resolution:  $0''.1/\text{pixel}$ ) have been used to sample the surrounding regions. Observations have been performed through filter F255W (medium UV) in order to efficiently select the BSS and horizontal branch (HB) populations, and through filters F336W (approximately corresponding to an  $U$  filter) and F555W ( $V$ ) for the red giant branch (RGB) population and to guarantee a proper combination with the ground-based data set (see below). The photometric reduction of the high-resolution images was carried out using ROMAFOT (Buonanno et al. 1983), a package developed to perform accurate photometry in crowded fields and specifically optimized to handle under-sampled Point Spread Functions (PSFs; Buonanno & Iannicola 1989), as in the case of the HST-WF chips.

To obtain a better coverage of the innermost regions of the cluster, we have also used a set of public HST-WFPC2 and HST-ACS observations. The HST-WFPC2 data set has been obtained through filters F439W ( $B$ ) and F555W ( $V$ ) by Piotto et al. (2002), and because of the different orientation of the camera, it is complementary to ours. Additional HST-ACS data in filters F435W ( $B$ ), F606W ( $V$ ), and F814W ( $I$ ) have been retrieved from the ESO-STECF Science Archive, and have been used to sample the central area not covered by the WFPC2 observations. All the ACS images were properly corrected for geometric distortions and effective flux (over the pixel area) following the prescriptions of Sirianni et al. (2005). The photometric analysis was performed independently in the three drizzled images by using the aperture photometry code SExtractor (*Source-Extractor*; Bertin & Arnouts 1996), and adopting a fixed aperture radius of 2.5 pixels ( $0.125''$ ). The magnitude lists were finally cross-correlated in order to obtain a combined catalog. The adopted combination of the three HST data sets is sketched in Figure 1 and provided a good coverage of the cluster up to  $r = 115''$ .

2. *The wide-field set* – A complementary set of wide-field  $B$  and  $V$  images was secured by using the Wide Field Imager (WFI) at the 2.2m ESO-MPI telescope during an observing run in April 2000. Thanks to the exceptional imaging capabilities of WFI (each image consists of a mosaic of 8 CCDs, for a global field of view of  $34' \times 34'$ ), these data cover the entire cluster

extension (see Figure 2, where the cluster is roughly centered on CCD #7). The raw WFI images were corrected for bias and flat field, and the overscan regions were trimmed using IRAF<sup>2</sup> tools. The PSF fitting procedure was performed independently on each image using DoPhot (Schechter, Mateo & Saha 1993). All the uncertain detections, usually caused by photometric blends, stars near the CCD gaps or saturated stars, have been checked one by one using ROMAFOT (Buonanno et al. 1983).

## 2.2. Astrometry and center of gravity

The HST+WFI catalog has been placed on the absolute astrometric system by adopting the procedure already described in Ferraro et al. (2001, 2003). The new astrometric Guide Star Catalog (GSC-II<sup>3</sup>) was used to search for astrometric standard stars in the WFI field of view (FoV), and a cross-correlation tool specifically developed at the Bologna Observatory (Montegriffo et al. 2003, private communication) has been employed to obtain an astrometric solution for each of the 8 CCDs. Several hundred GSC-II reference stars were found in each chip, thus allowing an accurate absolute positioning of the stars. Then, a few hundred stars in common between the WFI and the HST FoVs have been used as secondary standards to place the HST catalog on the same absolute astrometric system. At the end of the procedure the global uncertainties in the astrometric solution are of the order of  $\sim 0''.2$ , both in right ascension ( $\alpha$ ) and declination ( $\delta$ ).

Given the absolute positions of individual stars in the innermost regions of the cluster, the center of gravity  $C_{\text{grav}}$  has been determined by averaging coordinates  $\alpha$  and  $\delta$  of all stars lying in the PC FoV following the iterative procedure described in Montegriffo et al. (1995; see also Ferraro et al. 2003, 2004). In order to correct for spurious effects due to incompleteness in the very inner regions of the cluster, we considered two samples with different limiting magnitudes ( $m_{555} < 19.5$  and  $m_{555} < 20$ ), and we computed the barycenter of stars for each sample. The two estimates agree within  $\sim 1''$ , giving  $C_{\text{grav}}$  at  $\alpha(\text{J2000}) = 15^{\text{h}} 18^{\text{m}} 33^{\text{s}}.53$ ,  $\delta(\text{J2000}) = +2^{\circ} 4' 57''.06$ , with a  $1\sigma$  uncertainty of  $0''.5$  in both  $\alpha$  and  $\delta$ , corresponding to about 10 pixels in the PC image. This value of  $C_{\text{grav}}$  is located at  $\sim 4''$  south-west ( $\Delta\alpha = -4''$ ,  $\Delta\delta = -0''.9$ ) from that previously derived by Harris (1996) on the basis of the surface brightness distribution.

---

<sup>2</sup>IRAF is distributed by the National Optical Astronomy Observatory, which is operated by the Association of Universities for Research in Astronomy, Inc., under cooperative agreement with the National Science Foundation.

<sup>3</sup>Available at <http://www-gsss.stsci.edu/Catalogs/GSC/GSC2/GSC2.htm>.

### 2.3. Photometric calibration and definition of the catalogs

The optical HST magnitudes (i.e., those obtained through the WFPC2 filters F439W and F555W, and through ACS filters F435W, F606W, F814W), as well as the WFI  $B$  and  $V$  magnitudes have been all calibrated on the catalog of Sandquist et al. (1996). The UV magnitudes  $m_{160}$  and  $m_{255}$  have been calibrated to the Holtzman et al. (1995) zero-points following Ferraro et al. (1997, 2001), while the U magnitude  $m_{336}$  has been calibrated to Dolphin (2000).

In order to reduce spurious effects due to the low resolution of the ground-based observations in the most crowded regions of the cluster, we use only the HST data for the inner  $115''$ , this value being imposed by the FoV of the WFPC2 and ACS cameras (see Figure 1). In particular, we define as *HST sample* the ensemble of all the stars in the WFPC2 and ACS combined catalog having  $r \leq 115''$  from the center, and as *WFI sample* all stars detected with WFI at  $r > 115''$  (see Figure 2). The CMDs of the HST and WFI samples in the  $(V, U - V)$  and  $(V, B - V)$  planes are shown in Figure 3.

### 2.4. Density profile

We have determined the projected density profile over the entire cluster extension, from  $C_{\text{grav}}$  out to  $\sim 1400'' \sim 23'.3$ , by direct star counts, considering only stars brighter than  $V = 20$  (see Figure 3) in order to avoid incompleteness biases. The brightest RGB stars that are strongly saturated in the ACS data set have been excluded from the analysis, but since they are few in number, the effect on the resulting density profile is completely negligible. Following the procedure already described in Ferraro et al. (1999a, 2004), we have divided the entire HST+WFI sample in 27 concentric annuli, each centered on  $C_{\text{grav}}$  and split in an adequate number of sub-sectors. The number of stars lying within each sub-sector was counted, and the star density was obtained by dividing these values by the corresponding sub-sector areas. The stellar density in each annulus was then obtained as the average of the sub-sector densities, and its standard deviation was estimated from the variance among the sub-sectors.

The radial density profile thus derived is plotted in Figure 4, where we also show the best-fit mono-mass King model and the corresponding values of the core radius and concentration:  $r_c = 27''$  (with a typical error of  $\sim \pm 2''$ ) and  $c = 1.68$ , respectively. These values confirm that M5 has not yet experienced core collapse, and they are in good agreement with those quoted by McLaughlin & van der Marel (2005,  $r_c = 26''.3$  and  $c = 1.71$ ), and marginally consistent with those listed by Harris (1996,  $r_c = 25''.2$  and  $c = 1.83$ ), both derived from

the surface brightness profile. Our value of  $r_c$  corresponds to  $\sim 1$  pc assuming the distance modulus  $(m - M)_0 = 14.37$  ( $d \sim 7.5$  Kpc, Ferraro et al. 1999b).

### 3. DEFINITION OF THE SAMPLES

In order to study the BSS radial distribution and detect possible peculiarities, both the BSS and a reference population must be properly defined. Since the HST and the WFI data sets have been observed in different photometric bands, different selection boxes are needed to separate the samples in the CMDs. The adopted strategy is described in the following sections (see also Ferraro et al. 2004 for a detailed discussion of this issue).

#### 3.1. The BSS selection

At UV wavelengths BSS are among the brightest objects in a GC, and RGB stars are particularly faint. By combining these advantages with the high-resolution capability of HST, the usual problems associated with photometric blends and crowding in the high density central regions of GCs are minimized, and BSS can be most reliably recognized and separated from the other populations in the UV CMDs. For these reasons our primary criterion for the definition of the BSS sample is based on the position of stars in the  $(m_{255}, m_{255} - U)$  plane. In order to avoid incompleteness bias and the possible contamination from TO and sub-giant branch stars, we have adopted a limiting magnitude  $m_{255} = 18.35$ , roughly corresponding to 1 magnitude brighter than the cluster TO. This is also the limiting magnitude used by W06, facilitating the comparison with their study. The resulting BSS selection box in the UV CMD is shown in Figure 5. Once selected in the UV CMD, the bulk of the BSS lying in the field in common with the optical-HST sample has been used to define the selection box and the limiting magnitude in the  $(B, B - V)$  plane. The latter turns out to be  $B \simeq 17.85$ , and the adopted BSS selection box in the optical CMD is shown in Figure 6. The two stars lying outside the selection box (namely BSS-19 and BSS-20 in Table 1) have been identified as BSS from the  $(m_{255}, m_{255} - U)$  CMD. Indeed, they are typical examples of how the optical magnitudes are prone to blend/crowding problems, while the BSS selection in UV bands is much more secure and reliable. An additional BSS (BSS-47 in Table 1) lies near the edge of the ACS FoV and has only  $V$  and  $I$  observations; thus it was selected in the  $(V, V - I)$  plane (see Figure 7, where this BSS is shown together with the other 5 identified in the ACS complementary sample).

With these criteria we have identified 60 BSS: 47 BSS in the HST sample ( $r \leq 115''$ )

and 13 in the WFI one. Their coordinates and magnitudes are listed in Table 1. Out of the 47 BSS identified in the HST sample, 41 are from the WFPC2 data set, and 6 from the ACS catalog. As shown in Figure 1 their projected distribution is quite asymmetric with the N-E sector seemingly underpopulated. The statistical significance of such an asymmetry appears even higher if only the BSS outside the core are considered. However a quantitative discussion of this topic is not warranted unless additional evidences supporting this anomalous spatial distribution are collected. One of the inner BSS (BSS-29 in Table 1) lying at  $21''.76$  from the center, corresponds to the low-amplitude variable HST-V28 identified by Drissen & Shara (1998)<sup>4</sup>. In the WFI sample ( $r > 115''$ ) we find 13 BSS, with a more symmetric spatial distribution (see Figure 2). The most distant BSS (BSS-60 in Table 1, marked with an empty triangle in Fig.6) lies at  $\sim 24'$  from the center, i.e., beyond the cluster tidal radius. Hence, it might be an evaporating BSS previously belonging to the cluster. However, further investigations are needed before firmly assessing this issue.

In order to perform a proper comparison with W06 study, we have transformed their BSS catalog in our astrometric system, and we have found that 50 BSS of their bright sample lie at  $r \leq 115''$ : 35 are from the HST sample, 13 from the Canada France Hawaii Telescope (CFHT) data set, and 2 from the Cerro Tololo Inter-American Observatory (CTIO) sample; in the outer regions ( $115'' < r \lesssim 425''$ ) 9 BSS are identified, all from the CTIO data set.

By cross correlating W06 bright sample with our catalog we have found 43 BSS in common (see Table 1), 37 at  $r \leq 115''$  and 6 outward. In particular, 33 BSS out of the 41 (i.e., 80% of the total) that we have identified in the WFPC2-HST sample<sup>5</sup> are found in both catalogs, while 3 of our BSS belong to their faint BSS sample (namely, BSS-27, 34, and 40, corresponding to their Core BSS 70, 79, and 76, respectively), 5 of our BSS have been missed in W06 paper, and 2 objects in their sample are classified as HB stars in our study. This is probably due to different selection criteria, and/or small differences in the measured magnitudes, caused by the different data reduction procedures and photometric analysis. For example, W06 identify the BSS on the basis of both the UV and the optical observations, while we select the BSS only in the UV plane whenever possible. Out of the other 15 BSS found at  $r \leq 115''$  in the ground-based CFHT/CTIO sample of W06, 8 BSS (Core BSS 38–45 in their Table 2) clearly are false identifications. They are arranged in a very unlikely ring around a strongly saturated star, as can be seen in Figure 8, where the position in the sky of the 8 spurious BSS are overplotted on the CFHT image. Though they

---

<sup>4</sup>The observations presented here do not have the time coverage needed to properly search for BSS variability.

<sup>5</sup>Note that the WFPC2-HST observations used in W06 and in the present study are the same.



clearly are spurious identifications, they still define a clean sequence in the  $(B, B - I)$  CMD, nicely mimicking the BSS magnitudes and colors. As already discussed in previous papers, this once again demonstrates how automatic procedures for the search of peculiar objects are prone to errors, especially when using ground-based observations to probe very crowded stellar regions. We emphasize that all the candidate BSS listed in our Table 1 have been visually inspected evaluating the quality and the precision of the PSF fitting. This procedure significantly reduces the possibility of introducing spurious objects in the sample. Out of the remaining 7 BSS, 4 objects (namely their Core BSS 32, 30, 37 and 28) are also confirmed by our ACS observations (BSS-42, 43, 44, and 45 respectively), while 2 others (their Core BSS 27 and Ground BSS 6) are not found in the ACS data set, and the remaining one (their Ground BSS 7) is not included in our observation FoV. In turn, two BSS identified in our ACS data set (BSS 46 and 47) are missed in their sample. Concerning the BSS lying at  $115'' < r < 450''$ , 6 objects (out of 9 found in both samples) are in common between the two catalogs (see Table 1), one (BSS-55) belongs to W06 faint sample (their Ground BSS 23), while the remaining 2 do not coincide. Moreover, 4 additional BSS have been identified at  $r > 450''$  in our study.

### 3.2. The reference population

Since the HB sequence is bright and well separable in the UV and optical CMDs, we chose these stars as the primary representative population of normal cluster stars to be used for the comparison with the BSS data set. As with the BSS, the HB sample was first defined in the  $(m_{255}, m_{255} - U)$  plane, and the corresponding selection box in  $(B, B - V)$  has then been determined by using the stars in common between the UV and the optical samples. The resulting selection boxes in both diagrams are shown in Figures 5 and 6, and are designed to include the bulk of HB stars<sup>6</sup>. Slightly different selection boxes would include or exclude a few stars only without affecting the results.

We have used WFI observations to roughly estimate the impact of possible foreground field stars contamination on the cluster population selection. As shown in the right-hand panel of Figure 6, field stars appear to define an almost vertical sequence at  $0.4 < B - V < 1$  in the  $(B, B - V)$  CMD. Hence, they do not affect the BSS selection box, but marginally contaminate the reddest end of the HB. In particular, 5 objects have been found to lie within the adopted HB box in the region at  $r > r_t$  sample by our observations ( $\sim 194$  arcmin<sup>2</sup>); this corresponds to 0.026 spurious HB stars per arcmin<sup>2</sup>. On the basis of this, 11 field stars

---

<sup>6</sup>The large dispersion in the redder HB stars arises because RR Lyrae variables are included.

are expected to "contaminate" the HB population over the sampled cluster region ( $r < r_t$ ).

#### 4. THE BSS RADIAL DISTRIBUTION

The radial distribution of BSS in M5 has been studied following the same procedure previously adopted for other clusters (see references in Ferraro 2006; Beccari et al. 2006).

First, we have compared the BSS cumulative radial distribution to that of HB stars. A Kolmogorov-Smirnov test gives a  $\sim 10^{-4}$  probability that they are extracted from the same population (see Figure 9). BSS are more centrally concentrated than HB stars at  $\sim 4\sigma$  level.

For a more quantitative analysis, the surveyed area has been divided into 8 concentric annuli, with radii listed in Table 2. The number of BSS ( $N_{\text{BSS}}$ ) and HB stars ( $N_{\text{HB}}$ ), as well as the fraction of sampled luminosity ( $L^{\text{samp}}$ ) have been measured in the 8 annuli and the obtained values are listed in Table 2. Note that HB star counts listed in the table are already decontaminated from field stars, according to the procedure described in Section 3.2 (1, 2, and 8 HB stars in the three outer annuli have been estimated to be field stars). The listed values have been used to compute the specific frequency  $F_{\text{BSS}}^{\text{HB}} \equiv N_{\text{BSS}}/N_{\text{HB}}$ , and the double normalized ratio (see Ferraro et al. 1993):

$$R_{\text{pop}} = \frac{(N_{\text{pop}}/N_{\text{pop}}^{\text{tot}})}{(L^{\text{samp}}/L_{\text{tot}}^{\text{samp}})}, \quad (1)$$

with  $\text{pop} = \text{BSS, HB}$ .

In the present study luminosities have been calculated from the surface density profile shown in Figure 4. The surface density has been transformed into luminosity by means of a normalization factor obtained by assuming that the value obtained in the core ( $r \leq 27''$ ) is equal to the sum of the luminosities of all the stars with  $V \leq 20$  lying in this region. The distance modulus quoted in Section 2.4 and a reddening  $E(B-V) = 0.03$  have been adopted (Ferraro et al. 1999b). The fraction of area sampled by the observations in each annulus has been carefully computed, and the sampled luminosity in each annulus has been corrected for incomplete spatial coverage (in the case of annuli 3 and 8; see Figures 1 and 2).

The resulting radial trend of  $R_{\text{HB}}$  is essentially constant with a value close to unity over the surveyed area (see Figure 10). This is just what expected on the basis of the stellar evolution theory, which predicts that the fraction of stars in any post-main sequence evolutionary stage is strictly proportional to the fraction of the sampled luminosity (Renzini & Fusi Pecci 1988). Conversely, BSS follow a completely different radial distribution. As shown in Figure 10 the specific frequency  $R_{\text{BSS}}$  is highly peaked at the cluster center (a

factor of  $\sim 3$  higher than  $R_{\text{HB}}$  in the innermost bin), decreases to a minimum<sup>7</sup> at  $r \simeq 10 r_c$ , and rises again outward. The same behavior is clearly visible also in Figure 11, where the population ratio  $N_{\text{BSS}}/N_{\text{HB}}$  is plotted as a function of  $r/r_c$ .

Note that the region between  $800''$  and  $r_t \simeq 1290''$  (and thus also BSS-59, that lies at  $r \simeq 995''.5$ ) has not been considered in the analysis, since our observations provide a poor sampling of this annulus: only 35% of its area, corresponding to  $\sim 0.4\%$  of the total sampled light, is covered by the WFI pointing. However, for sake of completeness, we have plotted in Figure 12 the corresponding value of  $F_{\text{BSS}}^{\text{HB}}$  even for this annulus (empty circle in the upper panel): as can be seen, there is a hint for a flattening of the BSS radial distribution in the cluster outskirts.

#### 4.1. Dynamical simulations

Following the same approach as Mapelli et al. (2004, 2006), we now exploit dynamical simulations to derive some clues about the BSS formation mechanisms from their observed radial distribution. We use the Monte-Carlo simulation code originally developed by Sigurdsson & Phinney (1995) and upgraded in Mapelli et al. (2004, 2006). In any simulation run we follow the dynamical evolution of  $N$  BSS within a background cluster, taking into account the effects of both dynamical friction and distant encounters. We identify as COL-BSS those objects having initial positions  $r_i \lesssim r_c$ , and as MT-BSS stars initially lying at  $r_i \gg r_c$  (this because stellar collisions are most probable in the central high-density regions of the cluster, while primordial binaries most likely evolve in isolation in the periphery). Within these two radial ranges, all initial positions are randomly generated following the probability distribution appropriate for a King model. The BSS initial velocities are randomly extracted from the cluster velocity distribution illustrated in Sigurdsson & Phinney (1995), and an additional natal kick is assigned to the COL-BSS in order to account for the recoil induced by the encounters. Each BSS has characteristic mass  $M$  and lifetime  $t_{\text{last}}$ . We follow their dynamical evolution in the cluster (fixed) gravitational potential for a time  $t_i$  ( $i = 1, N$ ), where each  $t_i$  is a randomly chosen fraction of  $t_{\text{last}}$ . At the end of the simulation we register the final positions of BSS, and we compare their radial distribution with the observed one. We repeat the procedure until a reasonable agreement between the simulated and the observed distributions is reached; then, we infer the percentage of collisional and mass-transfer BSS from the distribution of the adopted initial positions in the simulation.

For a detailed discussion of the ranges of values appropriate for these quantities and

---

<sup>7</sup>Note that no BSS have been found between  $3.5'$  and  $5'$ .

their effects on the final results we refer to Mapelli et al. (2006). Here we only list the assumptions made in the present study:

- the background cluster is approximated with a multi-mass King model, determined as the best fit to the observed profile<sup>8</sup>. The cluster central velocity dispersion is set to  $\sigma = 6.5 \text{ km s}^{-1}$  (Dubath et al. 1997), and, assuming  $0.5 M_{\odot}$  as the average mass of the cluster stars, the central stellar density is  $n_c = 2 \times 10^4 \text{ pc}^{-3}$  (Pryor & Meylan 1993);
- the COL-BSS are distributed with initial positions  $r_i \leq r_c$  and are given a natal kick velocity of  $1 \times \sigma$ ;
- initial positions ranging between  $5 r_c$  and  $r_t$  (with the tidal radius  $r_t \simeq 48 r_c$ ) have been considered for MT-BSS in different runs;
- BSS masses have been fixed to  $M = 1.2 M_{\odot}$  (Ferraro et al. 2006a), and their characteristic lifetime to  $t_{last} = 2 \text{ Gyr}$ ;
- in each simulation run we have followed the evolution of  $N = 10,000$  BSS.

The simulated radial distribution that best reproduces the observed one (with a reduced  $\chi^2 \simeq 0.6$ ) is shown in Figure 11 (solid line) and is obtained by assuming that  $\sim 80\%$  of the BSS population was formed in the core through stellar collisions, while only  $\sim 20\%$  is made of MT-BSS. A higher fraction ( $\gtrsim 40\%$ ) of MT-BSS does not correctly reproduce the steep decrease of the distribution and seriously overpredict the number of BSS at  $r \sim 10 r_c$ , where no BSS at all are found, but it nicely matches the observed upturning point at  $r \simeq 13 r_c$  (see the dashed line in Figure 11). On the other hand, a population of only COL-BSS is unable to properly reproduce the external upturn of the distribution (see the dotted line in Figure 11), and 100% of MT-BSS is also totally excluded. Assuming heavier BSS (up to  $M = 1.5 M_{\odot}$ ) or different lifetimes  $t_{last}$  (between 1 and 4 Gyr) does not significantly change these conclusions, since both these parameters mainly affect the external part of the simulated BSS distribution. Thus, an appreciable effect can be seen only in the case of a relevant upturn, and negligible variations are found in the best-fit case and when assuming 100% COL-BSS. The effect starts to be relevant in the simulations with 40% or more MT-BSS, which are however inconsistent with the observations at intermediate radii (see above).

By using the simulations and the dynamical friction timescale (from, e.g., Mapelli et al. 2006), we have also computed the radius of avoidance of M5. This is defined as the characteristic radial distance within which all MT-BSS are expected to have already sunk to

---

<sup>8</sup>By adopting the same mass groups as those of Mapelli et al. (2006), the resulting value of the King dimensionless central potential is  $W_0 = 9.7$

the cluster core, because of mass segregation processes. Assuming 12 Gyr for the age of M5 (Sandquist et al. 1996) and  $1.2 M_{\odot}$  for the BSS mass, we find that  $r_{\text{avoid}} \simeq 10 r_c$ . This nicely corresponds to the position of the minimum in the observed BSS radial distribution, in agreement with the findings of Mapelli et al. (2004, 2006).

## 5. SUMMARY AND DISCUSSION

In this paper we have used a combination of HST UV and optical images of the cluster center and wide-field ground-based observations covering the entire cluster extension to derive the main structural parameters and to study the BSS population of the galactic globular cluster M5.

The accurate determination of the cluster center of gravity from the high-resolution data gives  $\alpha(\text{J2000}) = 15^{\text{h}} 18^{\text{m}} 33^{\text{s}}.53$ ,  $\delta(\text{J2000}) = +2^{\circ} 4' 57''.06$ , with a  $1\sigma$  uncertainty of  $0''.5$  in both  $\alpha$  and  $\delta$ . The cluster density profile, determined from direct star counts, is well fit by a King model with core radius  $r_c = 27''$  and concentration  $c = 1.68$ , thus suggesting that M5 has not yet suffered the core collapse.

The BSS population of M5 amounts to a total of 59 objects, with a quite asymmetric projected distribution (see Figure 1) and a high degree of segregation in the cluster center. With respect to the sampled luminosity and to HB stars, the BSS radial distribution is bimodal: highly peaked at  $r \lesssim r_c$ , decreasing to a minimum at  $r \simeq 10 r_c$ , and rising again outward (see Figures 10 and 11).

The comparison with results of W06 has revealed that 43 (out of 59) bright BSS identified by these authors at  $r \lesssim 450''$  are in common with our sample. Moreover, 4 additional stars classified as faint BSS in their study are in common with our BSS sample at  $r \lesssim 450''$ . Considering that we find 56 BSS within the same radial distance from the center, this corresponds to 84% matching of our catalogue. The discrepancies are explained by different data reduction procedures, photometric analysis, and adopted selection criteria, other than the spurious identification of 8 BSS by W06, due a strongly saturated star in their sample. The central peak of the  $R_{\text{BSS}}$  distribution in our study is slightly higher (but compatible within the error bar) compared to that of W06, and we extend the analysis to larger distance from the center (out to  $r > 800''$ ), thus unveiling the external upturn and the possible flattening of the BSS distribution in the cluster outskirts.

Moreover, we have compared the BSS radial distribution of M5 with that observed in other GCs studied in a similar way. In Figure 12 we plot the specific frequency  $F_{\text{BSS}}^{\text{HB}}$  as a function of  $(r/r_c)$  for M5, M3, 47 Tuc, and NGC 6752. Such a comparison shows

that the BSS radial distributions in these clusters are only *qualitatively* similar, with a high concentration at the center and an upturn outward. However, significant quantitative differences are apparent: (1) the  $F_{\text{BSS}}^{\text{HB}}$  peak value, (2) the steepness of the decreasing branch of the distribution, (3) the radial position of the minimum (marked by arrows in the figure), and (4) the extension of the “zone of avoidance,” i.e., the intermediate region poorly populated by BSS. In particular M5 shows the smallest  $F_{\text{BSS}}^{\text{HB}}$  peak value: it turns out to be  $\sim 0.24$ , versus a typical value  $\gtrsim 0.4$  in all the other cases. It also shows the mildest decreasing slope: at  $r \approx 2r_c$  the specific frequency in M5 is about a half of the peak value, while it decreases by a factor of 4 in all the other clusters. Conversely, it is interesting to note that the value reached by  $F_{\text{BSS}}^{\text{HB}}$  in the external regions is  $\sim 50\text{-}60\%$  of the central peak in all the studied clusters. Another difference between M5 and the other systems concerns the ratio between the radius of avoidance and the tidal radius:  $r_{\text{avoid}} \simeq 0.2r_t$  for M5, while  $r_{\text{avoid}} \lesssim 0.13r_t$  for 47 Tuc, M3, and NGC 6752 (see Tables 1 and 2 in Mapelli et al. 2006).

The dynamical simulations discussed in Section 4.1 suggest that the majority of BSS in M5 are collisional, with a content of MT-BSS ranging between 20% and 40% of the overall population. This fraction seems to be smaller than that (40-50%) derived for M3, 47 Tuc and NGC 6752 by Mapelli et al. (2006), in qualitative agreement with the smaller value of  $r_{\text{avoid}}/r_t$  estimated for M5, which indicates that the fraction of cluster currently depopulated of BSS is larger in this system than in the other cases. More in general, the results shown in Figure 11 exclude a pure collisional BSS content for M5.

Our study has also revealed the presence of a candidate BSS at  $\sim 24'$  from the center, i.e., beyond the cluster tidal radius (see Figures 2 and 6 and BSS-59 in Table 1). If confirmed, this could represent a very interesting case of a BSS previously belonging to M5 and then evaporating from the cluster (a BSS kicked off from the core the because of dynamical interactions?).

This research was supported by Agenzia Spaziale Italiana under contract ASI-INAF I/023/05/0, by the Istituto Nazionale di Astrofisica under contract PRIN/INAF 2006, and by the Ministero dell’Istruzione, dell’Università e della Ricerca. RTR is partially funded by NASA through grant number GO-10524 from the Space Telescope Science Institute. We thank the referee E. Sandquist for the careful reading of the manuscript and the useful comments and suggestions that significantly improved the presentation of the paper.

## REFERENCES

Albrow, M. D., et al. 2001, ApJ, 559, 1060

- Bailyn, C. D. 1994, *AJ*, 107, 1073
- Beccari, G., Ferraro, F. R., Lanzoni, B., & Bellazzini, M., 2006, *ApJ*, 652, L121
- Bellazzini, M., Fusi Pecci, F., Messineo, M., Monaco, L., & Rood, R. T. 2002, *AJ*, 123, 1509
- Bertin, E., & Arnouts, S. 1996, *A&AS*, 117, 393
- Buonanno, R., Buscema, G., Corsi, C. E., Ferraro, I., & Iannicola, G. 1983, *A&A*, 126, 278
- Buonanno, R., Iannicola, G. 1989, *PASP*, 101, 294
- Dolphin, A. E. 2000, *PASP*, 112, 1383
- Drissen, L., & Shara, M. M. 1998, *AJ*, 115, 725
- Dubath P., Meylan G., Mayor M., 1997, *A&A*, 324, 505
- Ferraro, F. R., Fusi Pecci, F., Cacciari, C., Corsi, C., Buonanno, R., Fahlman, G. G., & Richer, H. B. 1993, *AJ*, 106, 2324
- Ferraro, F. R., Paltrinieri, B., Fusi Pecci, F., Cacciari, C., Dorman, B., Rood, R. T., Buonanno, R., Corsi, C. E., Burgarella, D., & Laget, M., 1997, *A&A*, 324, 915
- Ferraro, F. R., Paltrinieri, B., Rood, R. T., Dorman, B. 1999a, *ApJ* 522, 983
- Ferraro F. R., Messineo M., Fusi Pecci F., De Palo M. A., Straniero O., Chieffi A., Limongi M. 1999b, *AJ*, 118, 1738
- Ferraro, F. R., D’Amico, N., Possenti, A., Mignani, R. P., & Paltrinieri, B. 2001, *ApJ*, 561, 337
- Ferraro, F. R., Sills, A., Rood, R. T., Paltrinieri, B., & Buonanno, R. 2003, *ApJ*, 588, 464
- Ferraro, F. R., Beccari, G., Rood, R. T., Bellazzini, M., Sills, A., & Sabbi, E. 2004, *ApJ*, 603, 127
- Ferraro, F. R., 2006, in *Resolved Stellar Populations*, ASP Conference Series, 2005, D. Valls-Gabaud & M. Chaves Eds., astro-ph/0601217
- Ferraro, F. R., et al. 2006a, *ApJ*, 647, L53
- Ferraro, F. R., Sollima, A., Rood, R. T., Origlia, L., Pancino, E., & Bellazzini, M. 2006b, *ApJ*, 638, 433

- Fusi Pecci, F., Ferraro, F. R., Corsi, C. E., Cacciari, C., Buonanno, R. 1992, *AJ*, 104, 1831
- Harris, W.E. 1996, *AJ*, 112, 1487
- Holtzman, J. A., Burrows, C. J., Casertano, S., Hester, J. J., Trauger, J. T., Watson, A. M., & Worthey, G. 1995, *PASP*, 107, 1065
- Lombardi, J. C. Jr., Rasio, F. A., Shapiro, S. L. 1995, *ApJ*, 445, L117
- Mapelli, M., Sigurdsson, S., Colpi, M., Ferraro, F. R., Possenti, A., Rood, R. T., Sills, A., & Beccari, G. 2004, *ApJ*, 605, L29
- Mapelli, M., Sigurdsson, S., Ferraro, F. R., Colpi, M., Possenti, A., & Lanzoni, B. 2006, *MNRAS*, 373, 361
- McLaughlin, D. E., & van der Marel, R. P. 2005, *ApJS*, 161, 304
- Montegriffo, P., Ferraro, F. R., Fusi Pecci, F., & Origlia, L. 1995, *MNRAS*, 276, 739
- Piotto, G., et al. 2002, *A&A*, 391, 945
- Pryor C., & Meylan G., 1993, *Structure and Dynamics of Globular Clusters*. Proceedings of a Workshop held in Berkeley, California, July 15-17, 1992, to Honor the 65th Birthday of Ivan King. Editors, S.G. Djorgovski and G. Meylan; Publisher, Astronomical Society of the Pacific, Vol. 50, 357
- Renzini, A., & Fusi Pecci, F. 1988, *ARA&A*, 26, 199
- Sabbi, E., Ferraro, F. R., Sills, A., Rood, R. T., 2004, *ApJ* 617, 1296
- Sandquist, E. L., Bolte, M., Stetson, P. B.; Hesser, J. E. 1996, *ApJ*, 470, 910
- Sarna, M. J., & de Greve, J. P. 1996, *QJRAS*, 37, 11
- Schechter, P. L., Mateo, M., & Saha, A. 1993, *PASP*, 105, 1342
- Shara, M. M., Saffer, R. A., & Livio, M. 1997, *ApJ*, 489, L59
- Sigurdsson S., Phinney, E. S., 1995, *ApJS*, 99, 609
- Sirianni, M., et al. 2005, *PASP*, 117, 1049
- Warren, S. R., Sandquist, E. L., & Bolte, M., 2006, *ApJ* 648, 1026 (W06)
- Zaggia, S. R., Piotto, G., & Capaccioli, M., 1997, *A&A*, 327, 1004



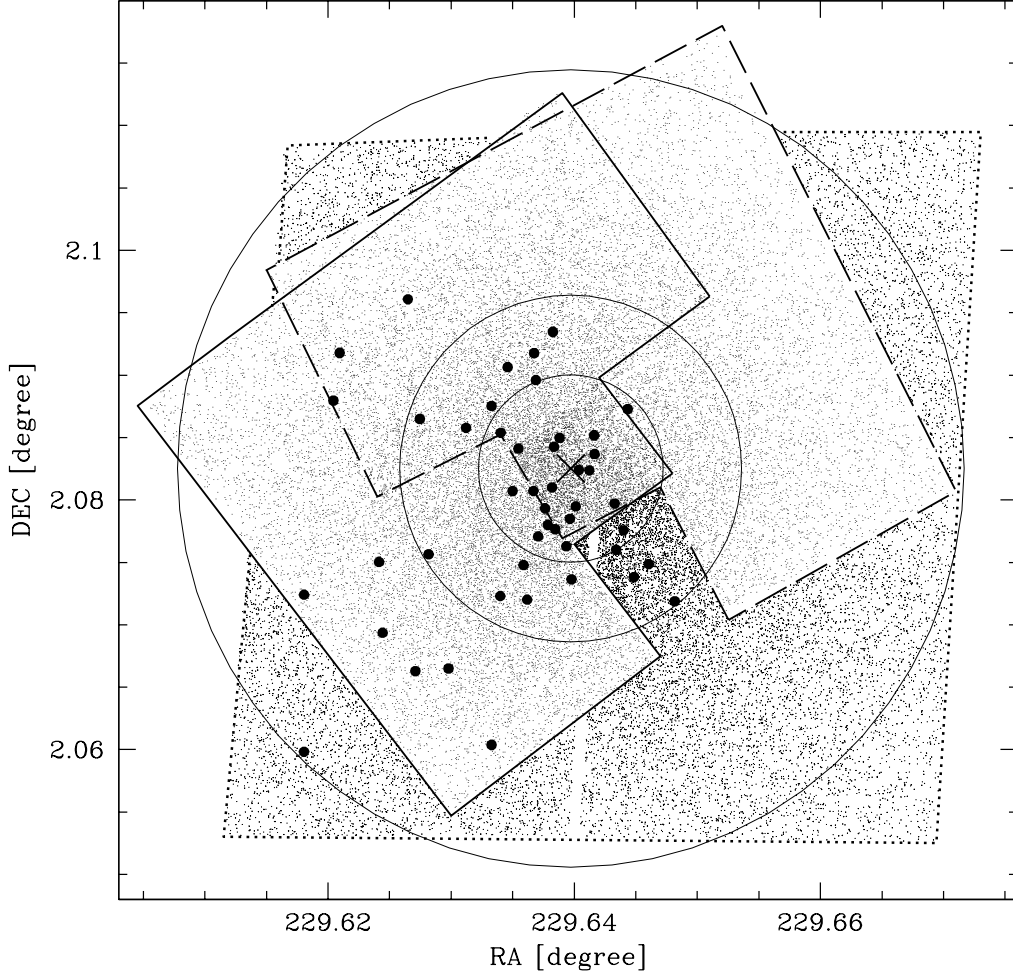


Fig. 1.— Map of the HST sample. The heavy solid line delimits the HST-WFPC2 FoV of our UV observations (Prop. 6607), the dashed line bounds the FoV of the optical HST-WFPC2 observations by Piotto et al. (2002), and the dotted line marks the edge of the complementary ACS data set. The derived center of gravity  $C_{\text{grav}}$  is marked with a cross. BSS (heavy dots) and the concentric annuli used to study their radial distribution (cfr. Table 2) are also shown. The inner and outer annuli correspond to  $r = r_c = 27''$  and  $r = 115''$ , respectively.

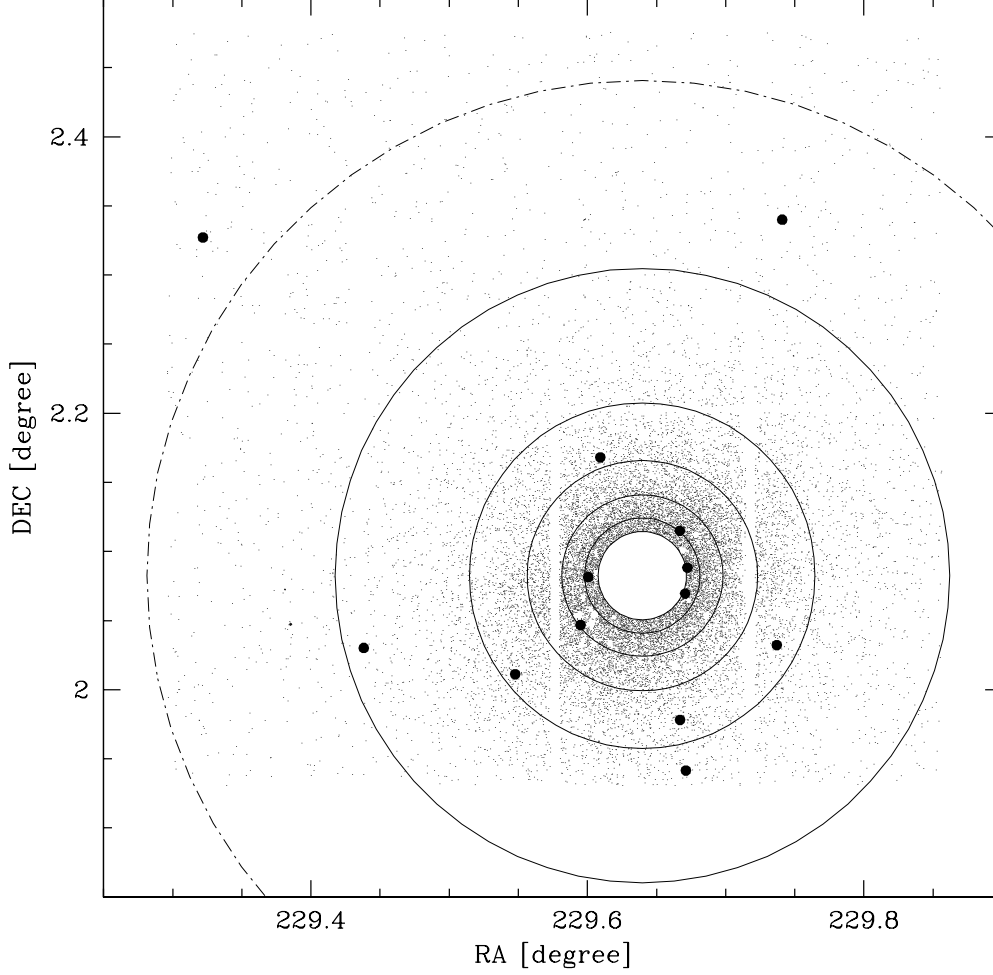


Fig. 2.— Map of the WFI sample. All BSS detected in the WFI sample are marked as heavy dots, and the concentric annuli used to study their radial distribution are shown as solid lines, with the inner and outer annuli corresponding to  $r = 115''$  and  $r = 800''$ , respectively (cfr. Table 2). The circle corresponding to the tidal radius ( $r_t \simeq 21'.5$ ) is also shown as dashed-dotted line. The BSS lying beyond  $r_t$  might represent a BSS previously belonging to M5 and now evaporating from the cluster.



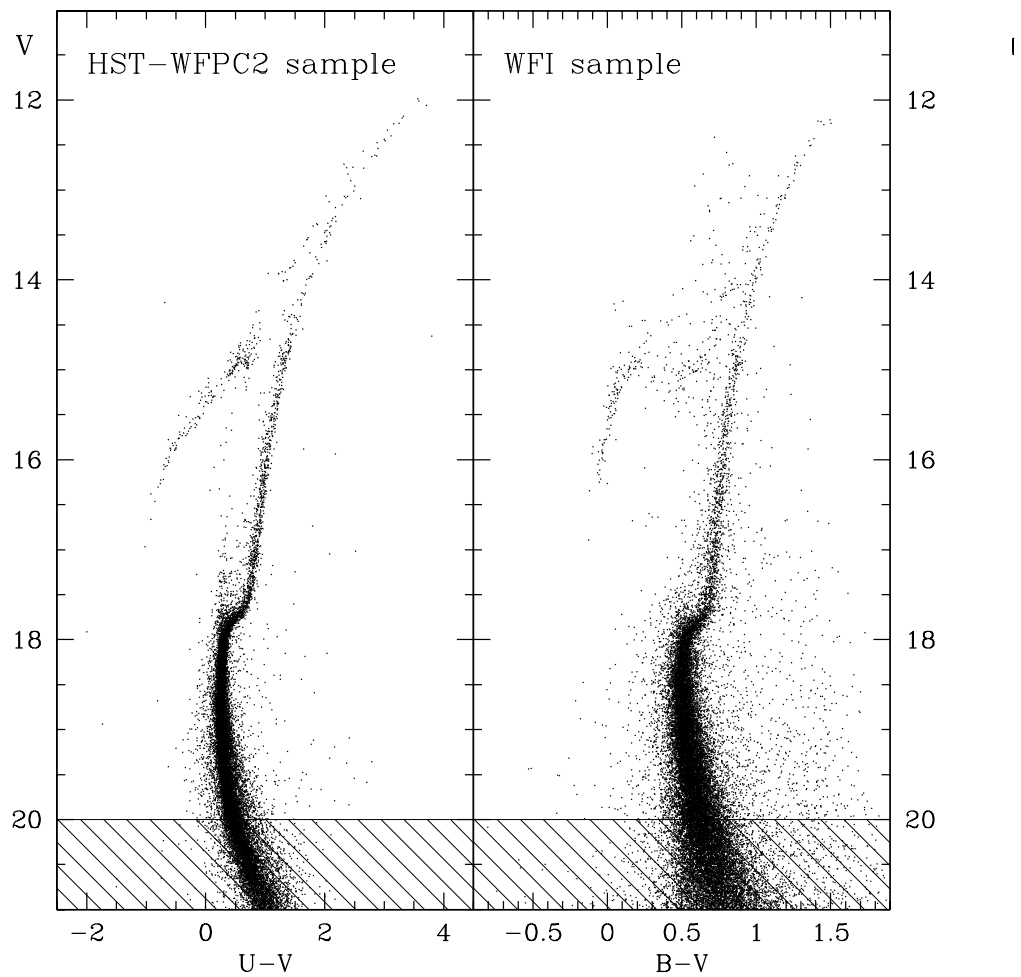


Fig. 3.— Optical CMDs of the WFPC2-HST and the WFI samples. The hatched regions indicate the magnitude limit ( $V \leq 20$ ) adopted for selecting the stars used to construct the cluster surface density profile.

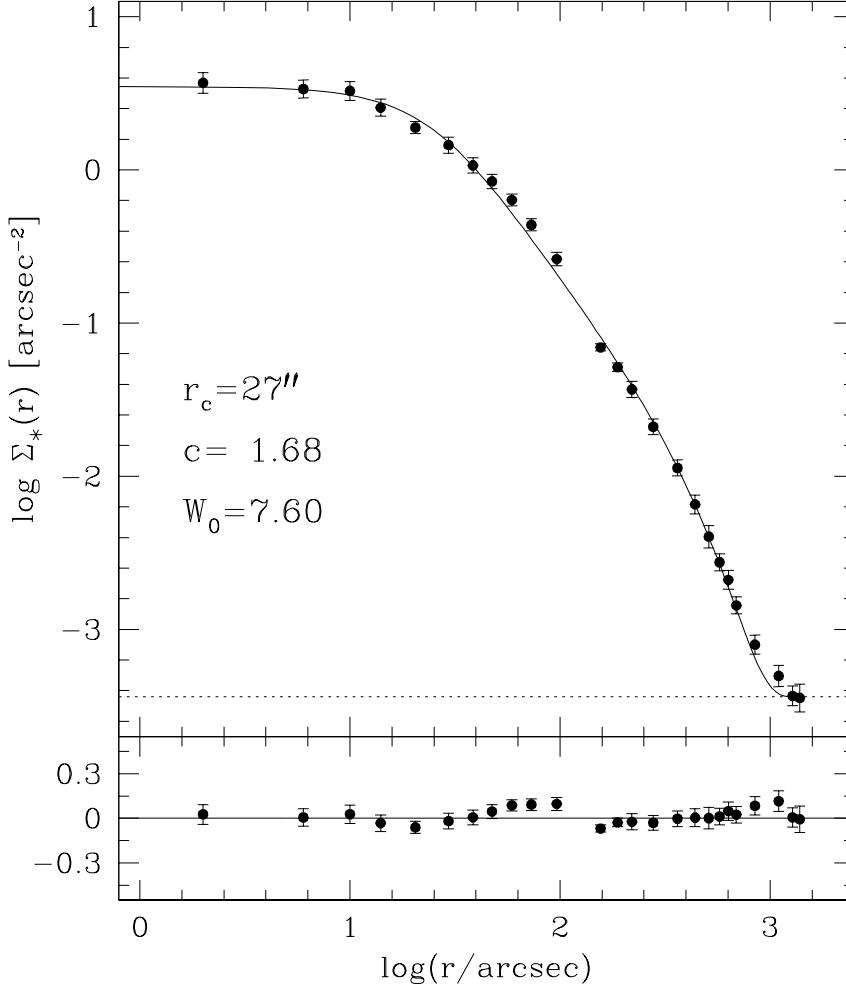


Fig. 4.— Observed surface density profile (dots and error bars) and best-fit King model (solid line). The radial profile is in units of number of stars per square arcseconds. The dotted line indicates the adopted level of the background, and the model characteristic parameters (core radius  $r_c$ , concentration  $c$ , dimensionless central potential  $W_0$ ) are marked in the figure. The lower panel shows the residuals between the observations and the fitted profile at each radial coordinate.

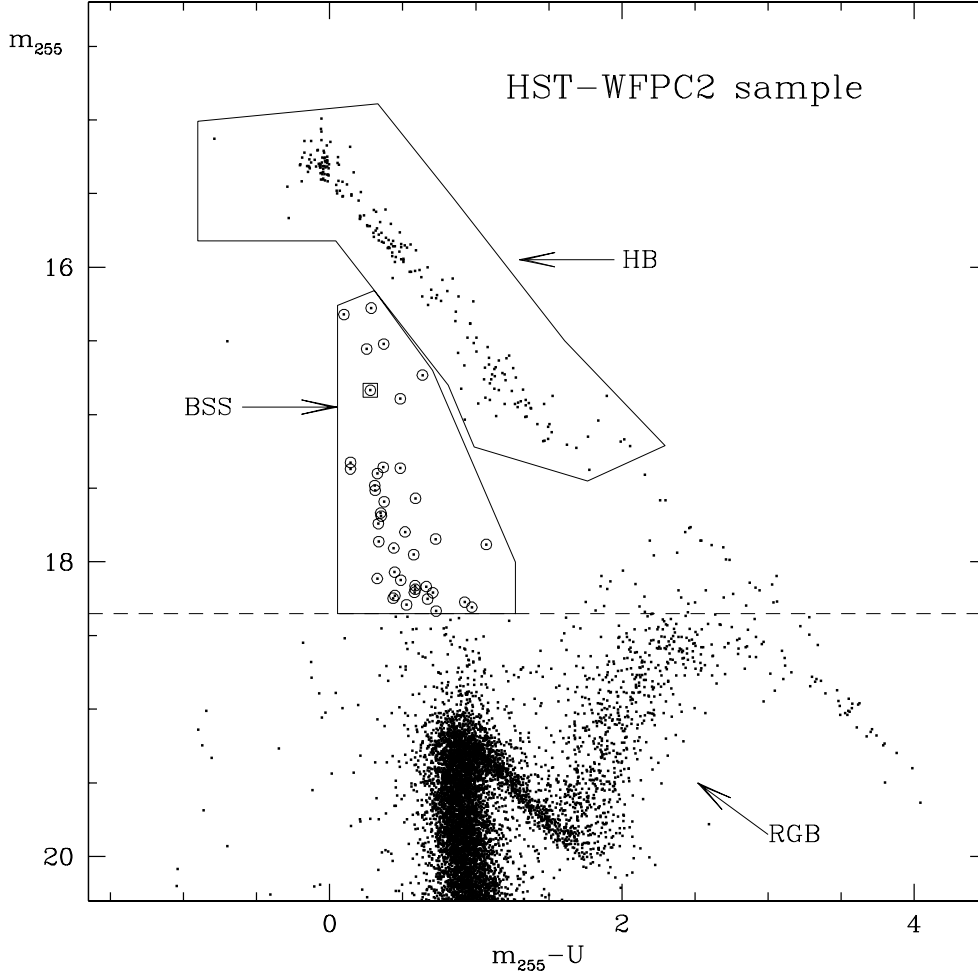


Fig. 5.— CMD of the ultraviolet HST sample. The adopted magnitude limit and selection box used for the definition of the BSS population are shown. The resulting fiducial BSS are marked with empty circles. The open square corresponds to the variable BSS identified by Drissen & Shara (1998). The box adopted for the selection of HB stars is also shown.

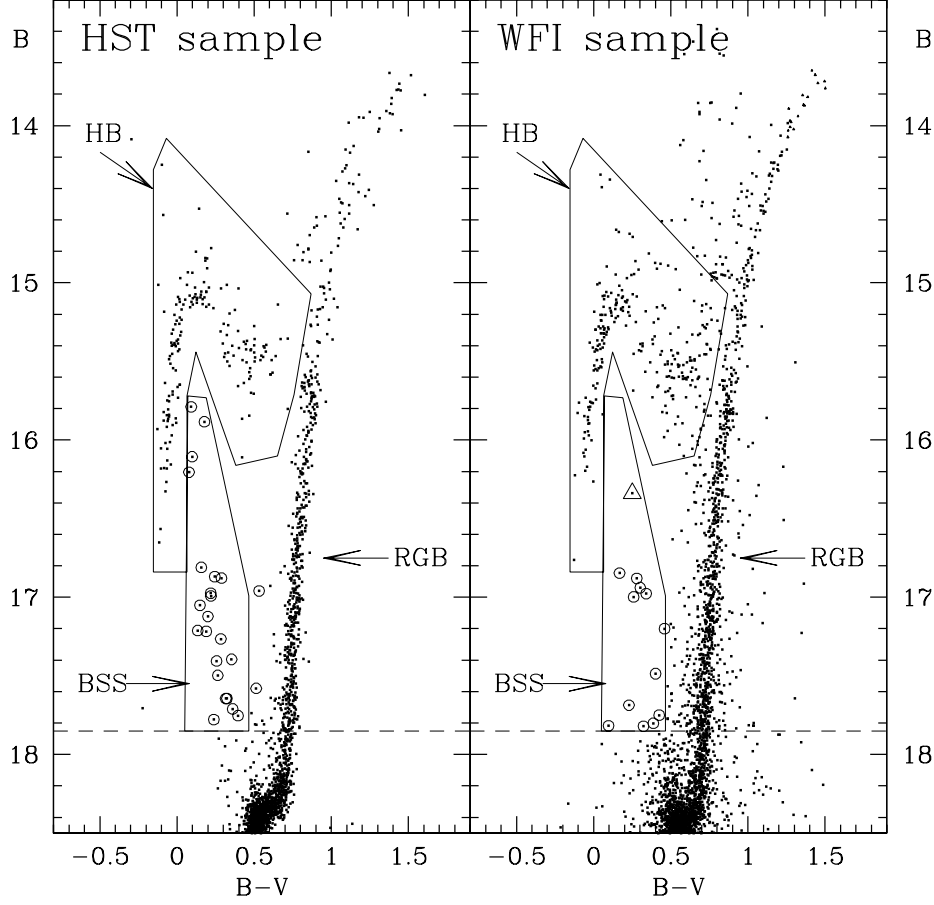


Fig. 6.— CMD of the optical HST-WFPC2 and WFI samples. The adopted BSS and HB selection boxes are shown, and all the BSS identified in these samples are marked with the empty circles. The two BSS not included in the box in the left-hand panel lie well within the selection box in the UV plane and are therefore considered as fiducial BSS. The empty triangle in the right-hand panel corresponds to the BSS identified beyond the cluster tidal radius, at  $r \simeq 24'$ .

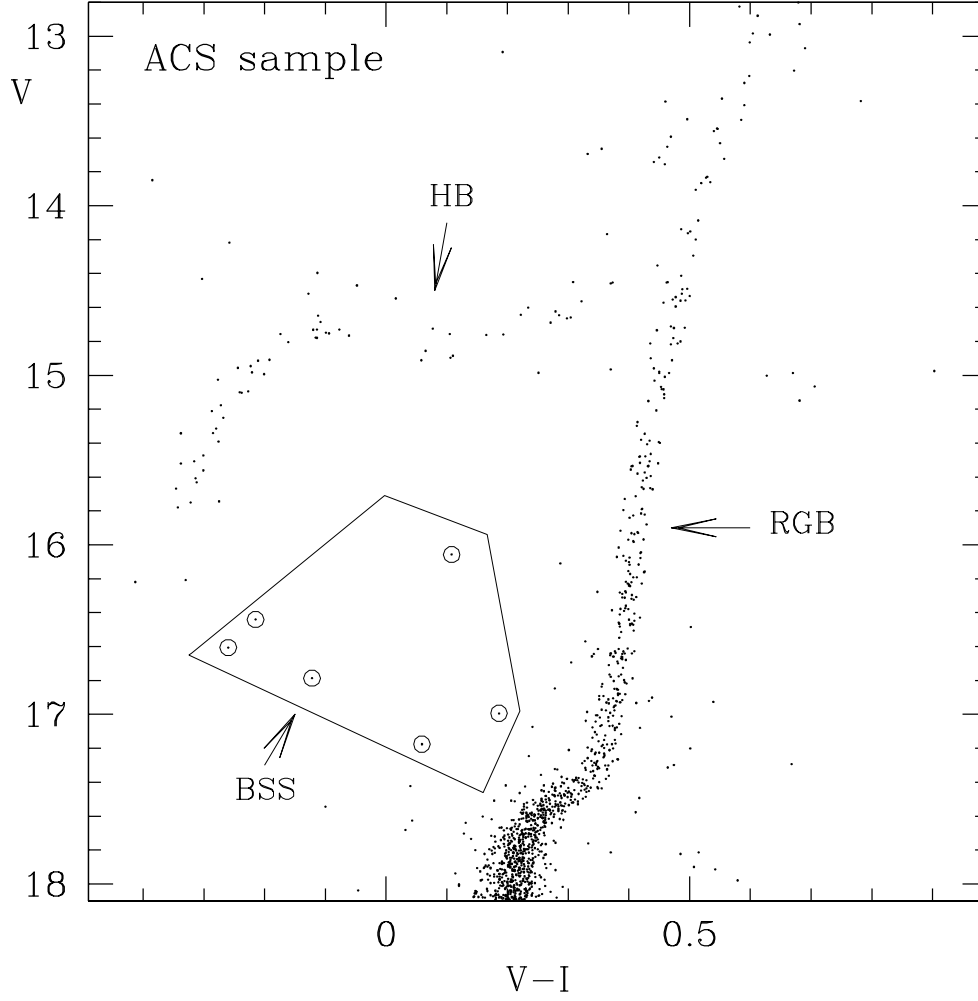


Fig. 7.— CMD of the ACS complementary sample. The BSS selection box is shown, and the resulting fiducial BSS are marked with empty circles.



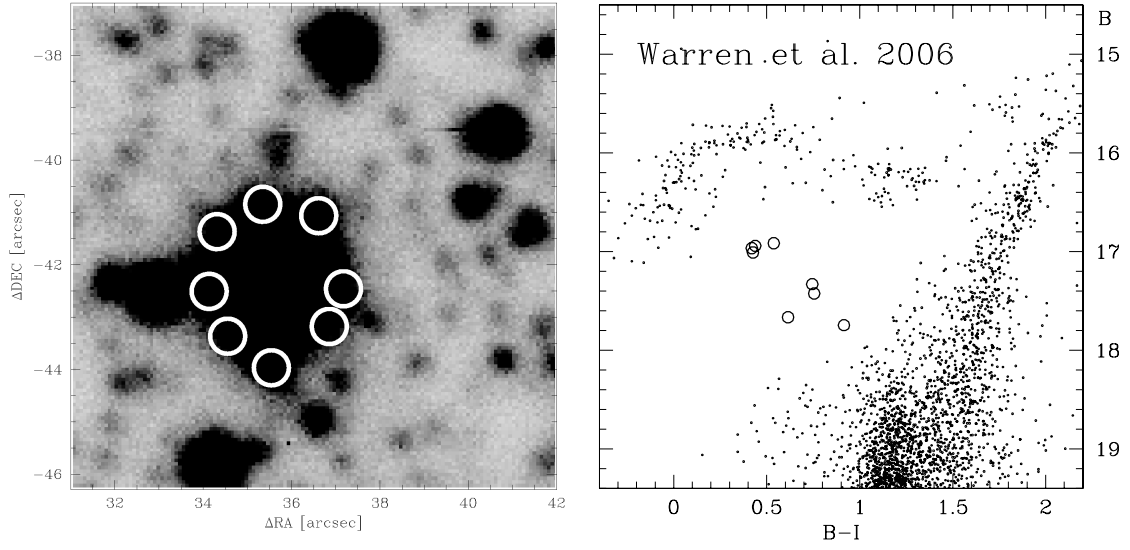


Fig. 8.— *Left-hand panel:* position of the 8 false BSS (marked with white circles) as derived from Table 2 of W06, overplotted to the CFHT image (units are the same as in their Figure 1). As can be seen, a heavily saturated star is responsible for the false identification. *Right-hand panel:* location of the 8 false BSS (empty circles) in the  $(B, B - I)$  plane, as derived from Table 2 of W06 (cfr. to their Fig. 2).

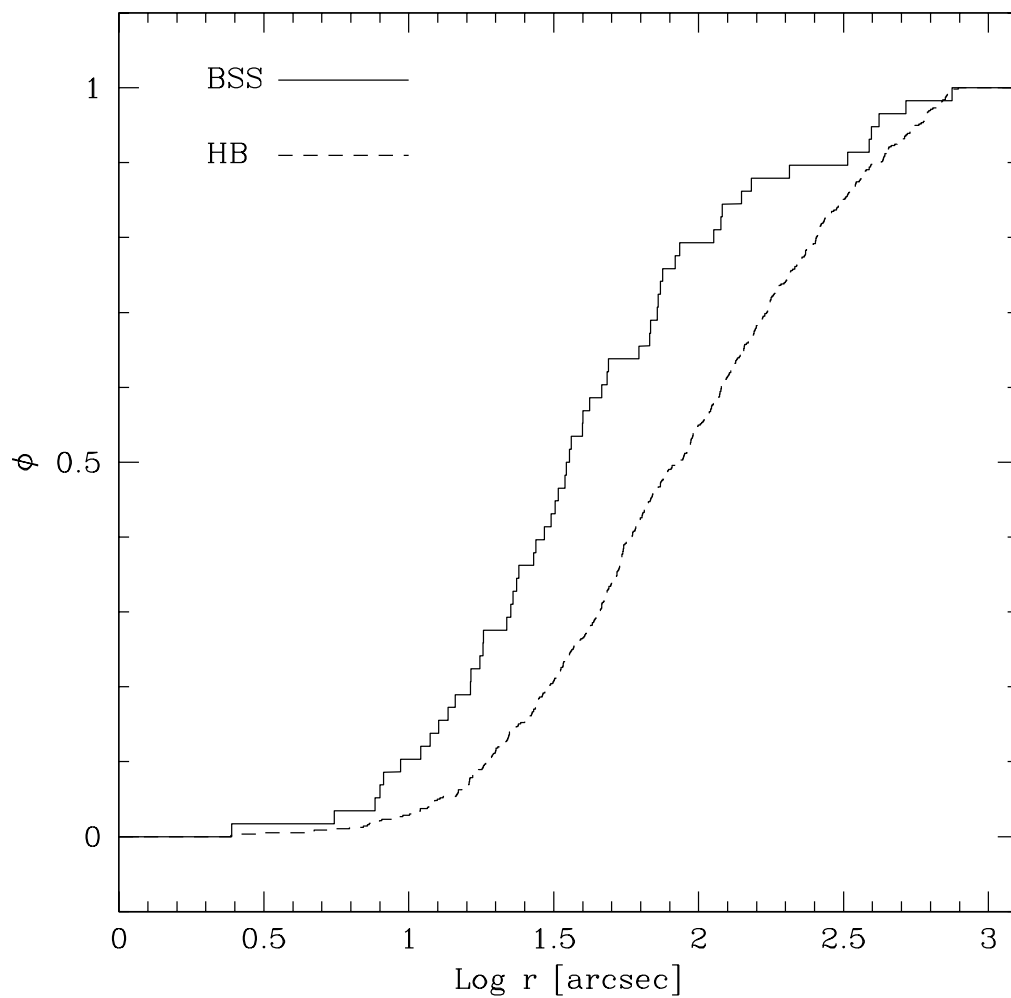


Fig. 9.— Cumulative radial distribution of BSS (solid line) and HB stars (dashed line) as a function of the projected distance from the cluster center for the combined HST+WFI sample. The two distributions differ at  $\sim 4\sigma$  level.

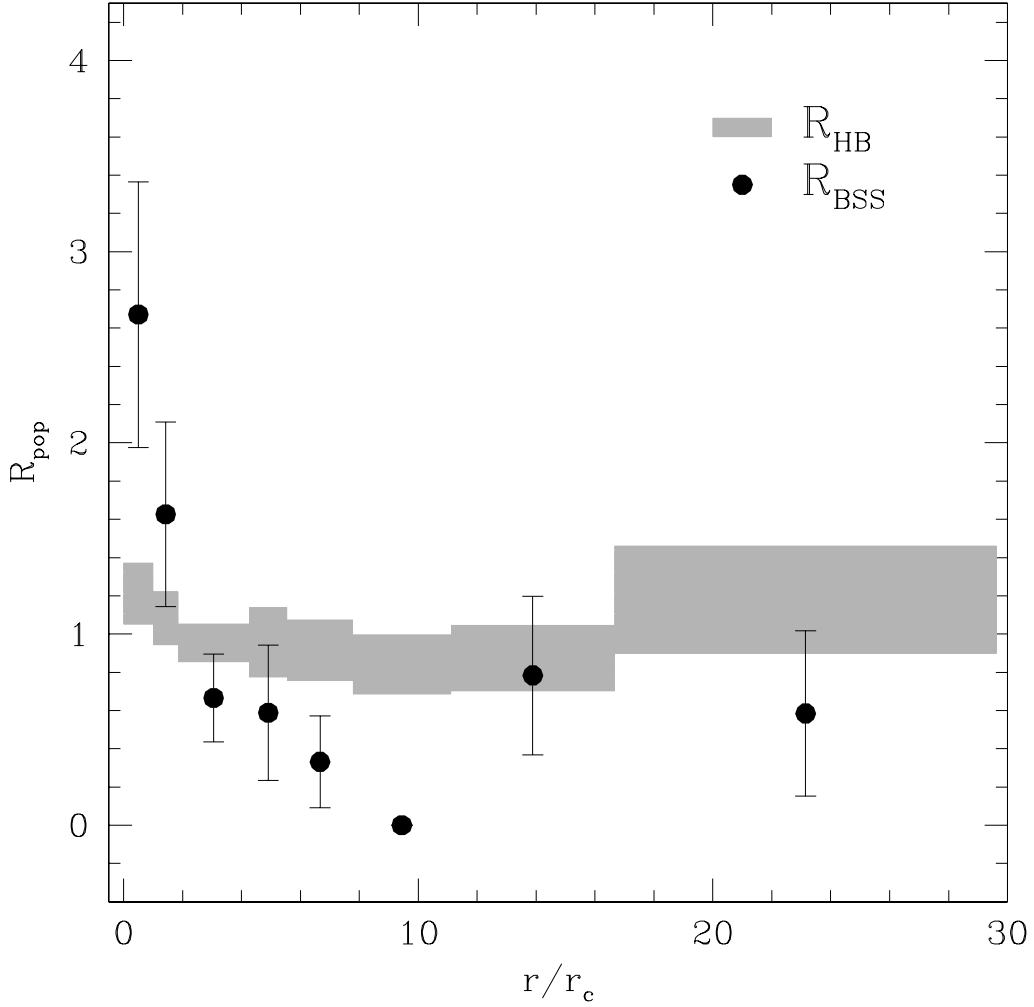


Fig. 10.— Radial distribution of the BSS and HB double normalized ratios, as defined in equation (1), plotted as a function of the radial coordinate expressed in units of the core radius.  $R_{\text{HB}}$  (with the size of the rectangles corresponding to the error bars computed as described in Sabbi et al. 2004) is almost constant around unity over the entire cluster extension, as expected for any normal, non-segregated cluster population. Instead, the radial trend of  $R_{\text{BSS}}$  (dots with error bars) is completely different: highly peaked in the center (a factor of  $\sim 3$  higher than  $R_{\text{HB}}$ ), decreasing at intermediate radii, and rising again outward.

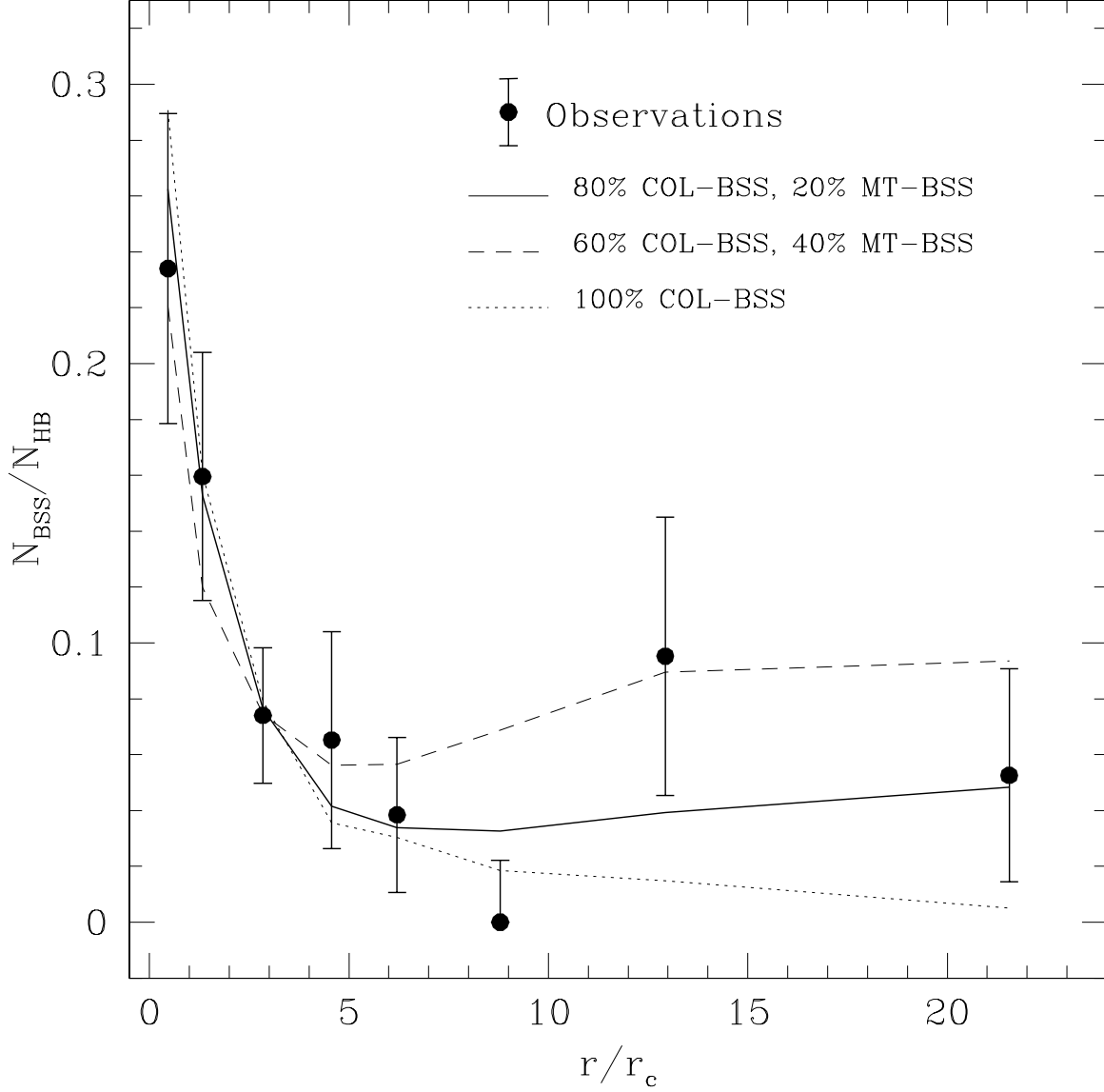


Fig. 11.— Observed radial distribution of the specific frequency  $N_{\text{BSS}}/N_{\text{HB}}$  (filled circles with error bars), as a function of  $r/r_c$ . The simulated distribution that best reproduces the observed one is shown as a solid line and is obtained by assuming 80% of COL-BSS and 20% of MT-BSS. The simulated distributions obtained by assuming 40% of MT-BSS (dashed line) and 100% COL-BSS (dotted line) are also shown.

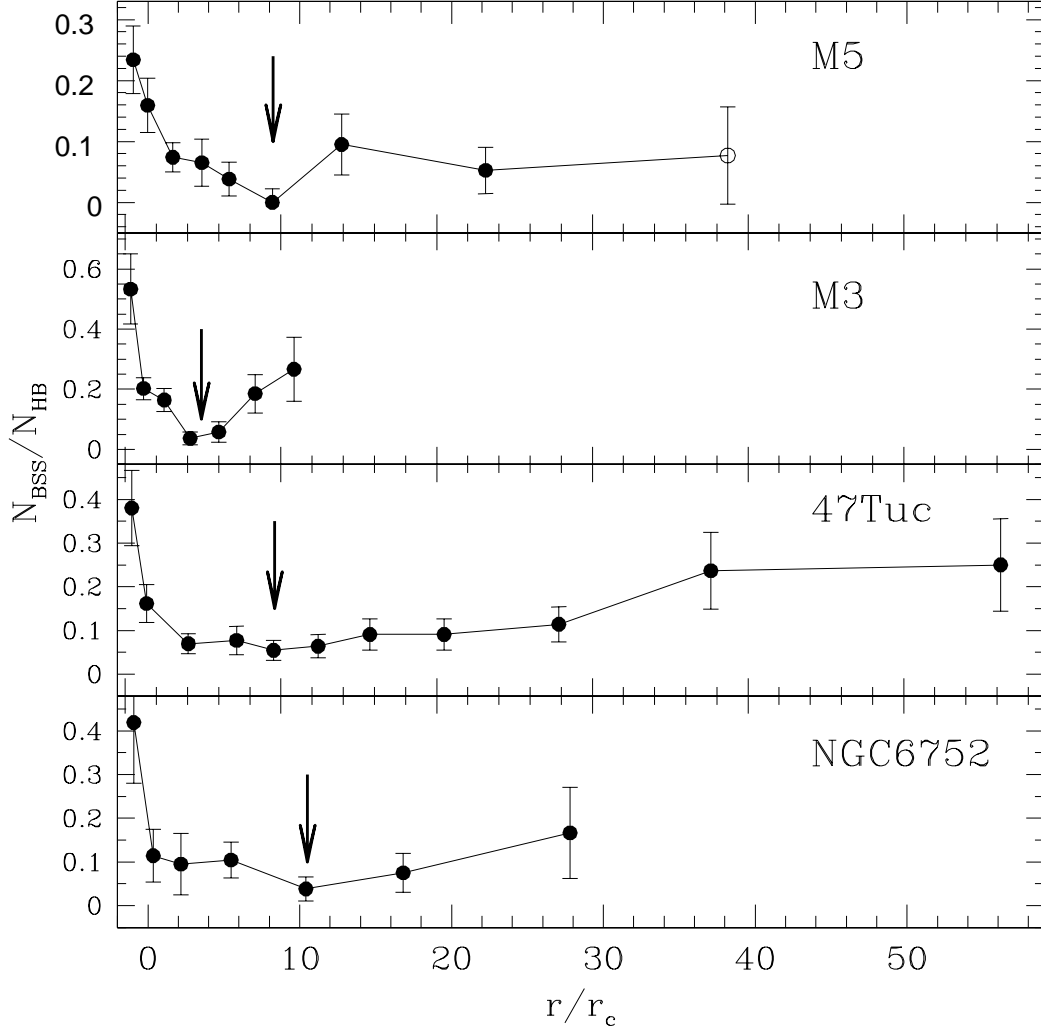


Fig. 12.— Radial distribution of the population ratio  $N_{\text{BSS}}/N_{\text{HB}}$  for M5, M3, 47 Tuc, and NGC 6752, plotted as a function of the radial distance from the cluster center, normalized to the core radius  $r_c$  (from Mapelli et al. 2006,  $r_c \simeq 30''$ ,  $21''$ ,  $28''$  for M3, 47 Tuc, and NGC 6752, respectively). The arrows indicate the position of the minimum of the distribution in each case. The outermost point shown for M5 (empty circle) corresponds to BSS-58, lying at  $r \simeq 995''$ . This star has not been considered in the quantitative study of the BSS radial distribution since only a negligible fraction of the annuli between  $800''$  and  $r_t$  is sampled by our observations.

Table 1. The BSS population of M5

Name	RA	DEC	$m_{255}$	U	B	V	I	W06
	[degree]	[degree]						
BSS-1	229.6354506	2.0841090	16.52	16.15	15.88	15.71	-	CR2
BSS-2	229.6388102	2.0849660	17.95	17.38	17.40	17.04	-	CR4
BSS-3	229.6383433	2.0842640	18.21	17.63	17.64	17.32	-	CR3
BSS-4	229.6416234	2.0851791	17.59	17.22	17.05	16.90	-	CR5
BSS-5	229.6416518	2.0836794	16.28	15.99	15.79	15.70	-	CR1
BSS-6	229.6381953	2.0810119	17.36	16.99	16.81	16.65	-	CR21
BSS-7	229.6403657	2.0824062	17.40	17.07	16.97	16.76	-	CR12
BSS-8	229.6412279	2.0823768	17.91	17.47	17.41	17.15	-	CR13
BSS-9	229.6376256	2.0793288	17.84	17.12	16.99	16.77	-	CR23
BSS-10	229.6401139	2.0794858	17.57	16.98	16.87	16.62	-	CR22
BSS-11	229.6396566	2.0784944	17.51	17.20	17.12	16.92	-	CR24
BSS-12	229.6432834	2.0797197	18.12	17.64	17.78	17.54	-	-
BSS-13	229.6384406	2.0776614	17.36	16.88	16.88	16.59	-	CR25
BSS-14	229.6274500	2.0864896	18.07	17.63	17.64	17.33	-	CR8
BSS-15	229.6204246	2.0879629	18.33	17.61	17.75	17.36	-	CR11
BSS-16	229.6209379	2.0917858	17.80	17.28	17.26	16.98	-	CR18
BSS-17	229.6264834	2.0960870	16.32	16.22	16.20	16.13	-	CR20
BSS-18	229.6368731	2.0896002	16.56	16.30	16.11	16.01	-	CR14
BSS-19	229.6367309	2.0917639	18.27	17.35	17.58	17.07	-	CR17
BSS-20	229.6345837	2.0906438	17.88	16.81	16.96	16.43	-	CR16
BSS-21	229.6382677	2.0934706	18.25	17.58	17.71	17.35	-	CR19
BSS-22	229.6340227	2.0853879	17.67	17.32	17.22	17.03	-	CR7
BSS-23	229.6332685	2.0875294	17.69	17.34	17.21	17.08	-	CR10
BSS-24	229.6366685	2.0807168	18.23	17.78	17.67	17.37	-	-
BSS-25	229.6393544	2.0762832	18.11	17.79	17.72	17.50	-	-
BSS-26	229.6378381	2.0779999	17.86	17.52	17.43	17.27	-	-
BSS-27	229.6349851	2.0807202	18.17	17.51	17.74	17.30	-	CR70
BSS-28	229.6397645	2.0736403	18.19	17.60	17.69	17.28	-	CR33
BSS-29	229.6370495	2.0770798	16.83	16.56	16.57	17.75	-	CR26
BSS-30	229.6358816	2.0747883	18.25	17.81	17.79	17.51	-	CR31
BSS-31	229.6361653	2.0720147	18.29	17.77	17.81	17.47	-	CR36
BSS-32	229.6339822	2.0723032	16.73	16.10	16.16	15.95	-	CR35
BSS-33	229.6281392	2.0756490	17.74	17.41	17.22	17.09	-	CR29
BSS-34	229.6241278	2.0750261	18.21	17.50	17.65	17.27	-	CR79
BSS-35	229.6332759	2.0603761	17.48	17.17	16.95	16.86	-	CR48
BSS-36	229.6270877	2.0662947	17.33	17.18	17.06	16.95	-	CR47
BSS-37	229.6244175	2.0693612	16.89	16.41	16.51	15.71	-	CR46
BSS-38	229.6180419	2.0724090	17.37	17.23	17.12	17.00	-	CR34

Table 1—Continued

BSS-39	229.6311963	2.0857800	18.31	17.33	17.40	16.76	-	-
BSS-40	229.6297499	2.0664961	18.16	17.58	-	17.27	-	CR76
BSS-41	229.6443367	2.0872809	-	-	17.50	17.23	-	CR9
BSS-42	229.6448646	2.0738335	-	-	16.53	16.06	15.95	CR32
BSS-43	229.6460645	2.0748695	-	-	16.64	16.44	16.66	CR30
BSS-44	229.6481631	2.0718829	-	-	16.72	16.61	16.87	CR37
BSS-45	229.6433942	2.0760163	-	-	17.03	16.79	16.91	CR28
BSS-46	229.6439884	2.0775670	-	-	17.44	16.99	16.81	-
BSS-47	229.6180420	2.0598328	-	-	-	17.18	17.12	-
BSS-48	229.6092873	2.1680914	-	-	16.85	16.68	-	OR2
BSS-49	229.6723094	2.0882827	-	-	16.94	16.64	-	OR9
BSS-50	229.6006551	2.0814678	-	-	17.00	16.74	-	OR10
BSS-51	229.6669956	1.9781808	-	-	17.20	16.74	-	OR1
BSS-52	229.5949935	2.0469325	-	-	17.69	17.46	-	OR4
BSS-53	229.6706625	2.0695464	-	-	17.82	17.50	-	-
BSS-54	229.6667908	2.1149550	-	-	17.82	17.72	-	-
BSS-55	229.7370667	2.0323392	-	-	17.80	17.42	-	OR23
BSS-56	229.5476990	2.0112610	-	-	16.88	16.60	-	OR5
BSS-57	229.6711255	1.9415566	-	-	16.98	16.64	-	-
BSS-58	229.4381714	2.0302088	-	-	17.75	17.33	-	-
BSS-59	229.7408412	2.3399166	-	-	17.49	17.08	-	-
BSS-60	229.3218200	2.3271022	-	-	16.34	16.09	-	-

Note. — The first 41 BSS have been identified in the WFPC2 sample; BSS-42–46 are from the complementary ACS observations; BSS-47–59 are from the WFI data-set. BSS-59 lies beyond the cluster tidal radius, at  $\sim 24'$  from the center. The last column list the corresponding BSS in W06 sample, with "CR" indicating their "Core BSS" and "OR" their "Outer Region BSS".

Table 2. Number counts of BSS and HB stars

$r_i''$	$r_e''$	$N_{\text{BSS}}$	$N_{\text{HB}}$	$L^{\text{samp}}/L_{\text{tot}}^{\text{samp}}$
0	27	22	94	0.14
27	50	15	94	0.16
50	115	10	135	0.26
115	150	3	46	0.09
150	210	2	52	0.10
210	300	0	45 <sup>†</sup>	0.10
300	450	4	42 <sup>†</sup>	0.09
450	800	2	38 <sup>†</sup>	0.06

Note. — <sup>†</sup> The  $N_{\text{HB}}$  values listed here are those corrected for field contamination (i.e., 1, 2 and 8 stars have been subtracted to the observed number counts in these three external annuli, respectively).